Research Square

Preprints are preliminary reports that have not undergone peer review.
They should not be considered conclusive, used to inform clinical practice,
or referenced by the media as validated information.

Key Role of Oxidising Species Driving Water Oxidation Revealed by Time Resolved Optical and X-ray Spectroscopies

Reshma Rao

reshma.rao@imperial.ac.uk

Imperial College London https://orcid.org/0000-0002-6655-3105

Caiwu Liang

Imperial College London

Lucas Verga

Imperial College London

Benjamin Moss

Imperial College London / California Institute of Technology

Santosh Kumar

Diamond Light Source

Soren Scott

University of Copenhagen https://orcid.org/0000-0002-1815-0141

Mark Turner

University of Manchester

Pilar Ferrer

Diamond Light Source https://orcid.org/0000-0001-9807-7679

Veronica Celorrio

Diamond Light Source

David Grinter

Diamond Light Source

Yemin Tao

Imperial College London

Sid Halder

Imperial College London

Yifeng Wang

Imperial College London

Cindy Tseng

Imperial College London

Guangmeimei Yang

Imperial College London

Georg Held

Diamond Light Source https://orcid.org/0000-0003-0726-4183

Sarah Haigh

The University of Manchester, Manchester, United Kingdom https://orcid.org/0000-0001-5509-6706

Aron Walsh

Imperial College London https://orcid.org/0000-0001-5460-7033

Ifan Stephens

Imperial College https://orcid.org/0000-0003-2157-492X

James Durrant

Imperial College London https://orcid.org/0000-0001-8353-7345

Article

Keywords:

Posted Date: August 6th, 2025

DOI: https://doi.org/10.21203/rs.3.rs-7022396/v1

License: This work is licensed under a Creative Commons Attribution 4.0 International License.
Read Full License

Additional Declarations: There is **NO** Competing Interest.

Version of Record: A version of this preprint was published at Nature Materials on February 26th, 2026. See the published version at https://doi.org/10.1038/s41563-026-02514-9.

Abstract

Oxidation states underpin the understanding of active states, reaction mechanisms, and catalytic performance of electrocatalysts. However, determining them—and the underlying physicochemical nature they reflect—at complex solid/liquid interfaces remains a challenge. Here, we use multimodal spectroscopy to investigate polarised iridium oxide (IrOx) electrodes, a model water-oxidation catalyst, to identify potential-dependent iridium and oxygen oxidation states and their implication on the active states and reaction mechanism for water oxidation. By integrating multiple operando spectroscopic techniques (optical (UV-vis), Ir L-edge, and O K-edge X-ray absorption spectroscopy) with electrochemistry mass spectrometry and density functional theory calculations, we identify a sequential depletion of electron densities from the Ir 5d band (corresponding to $Ir^{3+} \rightarrow Ir^{4+} \rightarrow Ir^{5+}$), followed by electron removal from the O 2p band, forming electrophilic oxygen species (O^{-1}) due to enhanced Ir-O covalency and electronic states overlap at higher applied potentials. Time-resolved measurements reveal distinct lifetimes for Ir5+ and O-1 states under water oxidation conditions, showing Ir5+ remains unreactive while O-1 is consumed, at a time constant commensurate with the reaction rate, consistent with the notion that O-1 drives the oxygen evolution reaction (OER). These findings thus demonstrate the necessity of using multiple advanced operando techniques to gain unified, mechanistic understanding of the evolution of oxidation states with potential and active states for water oxidation on oxide catalysts.

Main

The oxidation state of an element, originally tied to stoichiometric reactions of the element with oxygen, is defined as the net charge an atom would have if all bonding electrons in heteronuclear bonds were assigned to the more electronegative atom.[1] It is a cornerstone concept in chemical science, which has provided a straightforward way to understand and predict chemical bonding, redox reactions, and materials properties. In practice, atoms in solids often share their electron densities because bonding is seldom purely ionic;[2, 3] instead, it is generally heteropolar, exhibiting varying degrees of covalency and ionicity. As a result, connecting oxidation states to the observable electron density distribution in solid-state materials is often ambiguous.

Particularly in electrochemical systems, which inherently involve redox processes, assigning oxidation states and interpreting atomic charge can be complicated.[4, 5] In lithium batteries, for instance, the traditional view of transition-metal-centred redox processes for cathode materials (Li metal oxides) has expanded to include redox processes within the oxide lattice, where oxygen may deviate from its conventional -2 oxide state and exist in a -1 state. However, whether this oxygen -1 state arises from the formation of localised O–O dimers or other peroxo-like species—as would be implied by a simplified oxidation rule —or if it instead involves (de) localised holes on oxygen atoms within the metal oxide, is still an ongoing debate.[6-10] Nevertheless, understanding the precise nature of these oxygen states is crucial for controlling the reversibility of cathode materials and harnessing their extra capacity for next-generation, high-energy-density, long-life batteries.

The complexities determining oxidation states of elements in electrocatalysts are even more pronounced. Unlike battery materials, where redox processes typically occur within the bulk, electrocatalytic reactions take place at the surface, where local stoichiometry and electronic structure[11] often deviates from that of the bulk under reaction conditions.[12-14] The challenge of experimentally measuring surfaces at solid-liquid interfaces complicates the assignment of the species present and as a result, it limits insights into active states, reaction mechanisms and performance of catalysts.[15] Surface Pourbaix diagrams from density functional theory (DFT) calculations have enabled significant progress in understandings the evolution of surface adsorbates as a function of potential; however, they do not provide a detailed picture of how charges are distributed between the metal and ligand sites on the surface.[16-18]

Iridium oxides (IrO_x) have been extensively studied recently as water oxidation catalysts, since they exhibit both high activity[19] and stability[20, 21] and serve as a model system to understand reactivity at solid-liquid interfaces,[22-28] yet debate persists about the oxidation states under operating conditions and, more importantly, the active states that drive water oxidation. Prior synchrotron-based operando X-ray absorption spectroscopy (XAS) and X-ray photoelectron spectroscopy (XPS) studies have suggested the formation of Ir^{4+},[29] $Ir^{4.x+}$,[30] or Ir^{5+} species at oxygen evolution reaction (OER) potentials, with lower oxidation states acting as precursor species to OER.[31-33] Other reports even propose Ir^{6+}, analogous to the formal oxidations of iridium in some molecular iridium and double perovskite iridium oxides.[34, 35] In contrast, recent near-edge X-ray absorption fine structure (NEXAFS) studies have suggested a rather different active species––the formation of electrophilic oxygen species.[36-39] Note that the assignment of electron-deficient oxygen is primarily based on a characteristic ~529 eV feature in O K-edge spectra, with support from DFT simulations of spectra. However, the presence of this signal has been attributed to different physical origins in the literature. Strasser and co-workers, combining operando experiments and DFT on NiX (X = Fe, Mn, or Co) layer double hydroxide catalysts, assigned the ~529 eV signal to O ligands in the bulk after α-to-γ LDH transformation.[40] Similarly, Grimaud et al[41] linked the 528–529 eV feature in $H_{3.6}IrO_4 \cdot 3.7H_2O$ to structural water, noting that removing water from the structure significantly diminished the signal. A recent summary of O K-edge spectra suggested the ~529 eV signal could be due to highly oxidised states of iridium, which shifts the absorption of oxygen due to the covalent Ir–O bond.[42] These discrepancies in active-state assignments arise from the inherent ambiguity of charge distribution during electrochemical oxidation processes, which can involve the formation and presence of multiple species in the same OER potential range. This issue is further compounded by the fact that each spectroscopic technique offers only partial information, reflecting its specific operational focus and principles, while a molecular view of the interface demands the combination of multiple operando techniques and sufficient time-resolution to track the reactivity of the transient intermediates present at OER-relevant potentials.

Here, we combine multiple operando spectroscopic, mass spectrometry and theoretical methods to map the oxidation states of iridium oxides and thus to identify and quantify the active oxidising species that

drive water oxidation. First, we use quantum mechanical calculations to probe the electron-density distribution on surface atoms and adsorbates under varying potentials, linking these distributions to possible oxidation-state changes. We then integrate operando optical spectroscopy (based on our recent work[24]) with operando X-ray absorption spectroscopy at the Ir L-edge and O K-edge to track the oxidation-state evolution of both the metal centre and oxygen ligands. Time-resolved X-ray and optical spectroscopy are used to capture the dynamics of these states, illuminating their roles in the dynamic catalytic cycle. Using this multi-modal, time-resolved approach, we demonstrate that the surface oxidation at low potentials is dominated by the metal 5d states, while that at high potentials, corresponding to oxygen evolution reaction conditions, is dominated by the O 2p states, leading to the formation of electrophilic O^{-1} species. This species exhibits a time constant consistent with the overall reaction rate, suggesting its role as the key oxidising species driving OER. These insights provide a detailed molecular view of this water oxidation interface, and demonstrate the significance of the covalent nature of surface metal-oxide bonds in the formation of the active species for water oxidation.

Potential-dependent surface oxidation and localised charge density

Upon increasing the potential, changes in the surface oxygenated species can be predicted by surface Pourbaix diagrams (Fig. 1a, Table S1), calculated using density functional theory (DFT). This result is consistent with previously established surface Pourbaix diagrams.[16, 17, 24, 26, 27, 43-45] We also examined the impact of including Hubbard *U* corrections for Ir d-states, finding consistent structures across different potentials (Fig. S1). The change in surface structures, related to redox transitions, as also reported in our recent work,[24] are summarised as below (see details in Fig.1b and Supplementary Note 1):

Redox transition 1: $* H_2O_{CUS} + *H_{Bri} \rightarrow *OH_{CUS} + *H_{Bri} + H^+ + e^-$ (1)

Redox transition 2: $*OH_{CUS} + *H_{Bri} \rightarrow *OH_{CUS} + *_{Bri} + H^+ + e^-$ (2)

Redox transition 3: $*OH_{CUS} \rightarrow *O_{CUS} + H^+ + e^-$ (3)

Here, CUS refers to coordinatively unsaturated iridium sites, while Bri denotes bridge oxygen sites bonded to two adjacent iridium atoms. To investigate the possible changes in charge density associated with these surface structural transitions, we calculated the average changes in Bader charges for surface Ir and O atoms during each redox transition (Fig. 1b, Table S2 in Supplementary Note 1). Bader charges are obtained by dividing the electron density into atomic regions using surfaces where the gradient of the density is zero. The results indicate significant electron depletion predominantly occurring at Ir sites for redox transitions 1 and 2 (charge decreases of approximately -0.3 and -0.27 e^-, respectively). Conversely, at higher potentials (redox transition 3), electron depletion is primarily observed on O atoms. To further understand the surface electronic structure changes as a function of potential, we calculated the evolution of the average Ir 5d and O 2p band centers for the surface Ir (Fig. 1c). As the potential increases, the O 2p band center shifts upward from approximately −7.6 eV to

around −3.8 eV, while the Ir 5d band center shifts downward from approximately −3.9 eV to the range of −4.5 eV (See projected density of states for CUS and Bri sites respectively in Fig. S2). This indicates that at lower potential, the oxidation process depletes electron density from Ir 5d bands, leading to a shift in the Fermi level relative to the Ir 5d and O 2p bands. As the potential increases, both Ir 5d and O 2p bands are close to the Fermi level, thereby initiating electron extraction from the O 2p bands in the oxidation process (as schematically shown in the inset of Fig. 1c). This shift is also associated with enhanced Ir–O covalency under applied potential, consistent with our previous operando EXAFS studies showing a contraction of the Ir–O bond with increasing potential.[23]

Although the modelled single facet rutile IrO_2 (110) structure does not fully capture the complexity of practical IrO_x catalysts, these theoretical results suggest that oxidation processes on iridium oxides may involve both iridium and oxygen sites, and the dual-site participation in electron loss could complicate the definitive assignments of oxidation states and the mechanistic understanding of water oxidation—particularly in identifying the active states responsible for O–O bond formation (as schematically shown in Fig. 1a).

Determination of Ir and O oxidation using correlated spectroscopies

With theoretical evidence demonstrating that Ir and O could both be oxidised under anodic bias, we use a combination of operando optical (Fig. 2a), Ir L-edge (Fig. 2b) and O K-edge (Fig. 2c) spectroscopies to experimentally capture the changes in oxidation states of the iridium metal centres and oxygen ligands. Electrodeposited IrO_x thin films are used considering their volume active features—that is, the majority of the iridium centres are active in this structure.[24, 46] Transmission electron microscopy (TEM) analysis (Supplementary Note 2, Fig. S3) shows no evidence of crystallinity in these IrO_x films, consistent with our previous Extended X-ray Absorption Fine Structure analysis indicating that the material is composed of short-range ordered [IrO_6] octahedra.[24] These features enhance potential-induced spectroscopic signals and simplify the interpretation of results compared to other mixed-phase iridium-based catalysts or particle/ionomers systems.

Operando optical spectroscopy shows continuously increased absorbance across 450-850 nm wavelength as potential increases (Fig.2a). Following our previous work, these absorbance spectra can be deconvoluted into three different redox transitions according to their spectral shape, and their densities are quantified using Lambert-Beer law (depicted as light blue, orange and red lines in Fig. 2d, black y-axis, see details for deconvolution in Supplementary Note 2, Fig. S4-6). [23, 24] Similarly, operando Ir-L edge XANES shows that the white line position continuously shifts to higher energy with increasing potential from 0.6 V to ~1.4 V_{RHE} (Fig. 2b, as adapted from our previous work[23]), but remains roughly unchanged at higher potentials. This energy shift corresponds to an increase in the average iridium oxidation state from approximately +3.1 to +4.8, following the analysis in our previous work that shows around 1 eV shift per hole in the Ir 5d band [23] (depicted as blue triangles in Fig. 2d). Notably, at 0.6 V_{RHE}, the average Ir oxidation state can be reduced to as low as +3.1, in agreement with previous observations

that, in similar hydrous IrO_x, nearly all Ir sites can be electrochemically reduced from +4 to +3. [24, 46, 49] Interestingly, the potential dependence of the first two redox transitions detected via optical spectroscopy correlates well with the increase in Ir oxidation state (i.e. the light blue lines and orange line overlap well with blue triangles), thus corresponding to the oxidation of Ir^{3+} to Ir^{4+} and then Ir^{4+} to Ir^{5+}. Although the average Ir oxidation state reaches +4.8, slightly lower than +5, it is likely that the redox-accessible Ir sites are at +5, while a minor fraction remains at +3 or +4, resulting in the observed average values. This Ir^{5+} state is consistent with recent reports showing that various iridium oxide crystallinity and structures attain a surface oxidation state of Ir^{5+} at OER-relevant potentials.[31] Crucially, the final redox transition observed in optical spectroscopy, occurring in the OER regions, does not correspond to further oxidation of metallic Ir centre to higher oxidation states. Instead, as the Ir oxidation state plateaus, redox transition 3 emerges (red lines in Fig 2d). This observation suggests that there is an additional oxidation process where electrons are extracted without further oxidising the Ir metal centre.

To further understand the physicochemical nature of the final redox transitions, operando NEXAFS was used to examine changes in the oxygen ligands (see experimental details and cell design in Supplementary Note 4, Fig S7). The operando O K-edge spectra resemble those of pure water (inset of Fig. 2c) [47, 48] but display distinct features in the low-energy region from 527 eV to 532 eV associated with iridium oxides (Fig. 2c, Fig. S8-9). With increasing potential from open-circuit potential (OCP) to 1.49 V_{RHE}, there is a clear increase in absorption intensity between 528.5 and 530 eV, indicating a potential-driven alteration in oxygen species within iridium oxides. This observation aligns with findings from Pfeifer and Jones et al.[36-39] on iridium oxides and from Dorian et al.,[50] Koper et al. [51] and Strasser[40] on Ni-Fe based catalysts, where increased signal with potential is observed in similar energy regions. Pfeifer et al suggested that the broadened peak could be broken down into distinct peaks representing various oxygenate species. Using DFT calculations, they assigned the peak at around 529 eV to holes in oxygen 2p (labelled as O^{-1}) in bridge oxygen (μ_2-O) and adsorbed coordinated unsaturated (CUS) oxygen (μ_1-O), while the peak at around 530 eV is assigned to lattice O^{-2}.[37, 39] The following works from the same groups further suggested that μ_1-OH also shows absorption at around 529.5 eV, although signal from μ_1-OH is calculated to be weaker and likely more difficult to observed experimentally.[33, 52, 53] In contrast, Grimaud et. al.[41] assigned the signal in similar range on $H_xIrO_4 \cdot yH_2O$ to structural change. Recent work from Strasser also suggested that this signal on Ni oxides doesn't correlate to O^{-1} species, but instead is related to phase change.[40] The existence of O^{-1} species remains debated.

Considering the inconsistent assignment, rather than assigning specific peaks, we traced the signal at 529 eV—which may correlate to various oxygen features—as a function of potential during two cycles of cyclic voltammetry from 0.5 V_{RHE} to ~1.47 V_{RHE} (purple dots in Fig. 2d), and correlated it with Ir oxidation states and optically resolved redox transitions (see electrochemistry vs. oxygen fluorescence signal in Fig. S10). As shown in Fig. 2d, the oxygen XAS signal remains constant in the low potential range (0.5–0.85 V_{RHE}) but increases continuously at higher potential up to 1.47 V_{RHE}. This pattern contrasts with that of iridium, where iridium oxidation states increase from 0.6 to 1.4 V_{RHE} and plateau at potentials

above 1.4 V_{RHE}. Notably, the increase in XAS signal >1.40 V_{RHE} aligns well with the redox transition 3 resolved in optical spectroscopy, where the signal continues to increase even above 1.4 V_{RHE}.

These correlated spectroscopic results suggest that the electrons extracted during the final redox transitions might come from oxygen ligands, forming electron-deficient oxygen species O^{-1}. Notably, although the oxygen XAS signal also increases during redox transition 2, we attribute this to changes in the X-ray absorption of different oxygenated species (i.e. $*OH_{Bri} \rightarrow *O_{Bri} + H^+ + e^-$). The oxygen involved in redox transition 2 likely remains in a chemical state close to typical O^{-2}, as the observed charge transfer is primarily accounted for by changes in the oxidation state of iridium. Thus, by comparing Ir and O signals with optical spectroscopy across a wide range of potentials, our results seem to support the existence of O^{-1} at positive potentials. However, we acknowledge that steady-state XAS measurements have limited dynamic and potential resolution, and are susceptible to beam damage or time dependent changes during prolonged exposure,[10] which may introduce uncertainties in determining whether iridium oxidation truly plateaus and oxygen oxidation subsequently begins. To address this, we next traced the dynamic oxidation and reduction responses of iridium and oxygen to applied potential using time-resolved optical and X-ray spectroscopies.

Dynamics of iridium and oxygen oxidation

The dynamic response of the optical signal, Ir XAS and oxygen XAS signals to applied potentials are tracked as the potential steps up and down in different potential ranges. The ranges—around 0.6–0.8 V_{RHE} for redox transition 1, 1.1–1.3 V_{RHE} for redox transition 2, and 1.4–1.5 V_{RHE} for redox transition 3—were identified through deconvolution of optical absorption spectroscopy (see Fig. 2d). As shown in Fig. 3a, for all three redox transitions, the optical absorption signal responds rapidly and to the potential change. Similarly, the Ir XAS intensity at 11222 eV quickly rises and falls with the stepping up and down of potential in the potential ranges corresponding to redox transitions 1 and 2 (Fig. 3b). The Ir XAS intensity at 11222 eV is proportional to its oxidation states changes, as established by correlating the intensity with the oxidation states obtained in Fig. 2d. (see detailed discussion in Supplementary Note 5, Fig S11-12). However, in contrast, during redox transition 3 (1.44 to 1.5 V_{RHE}), the Ir XAS signal does not exhibit a rapid response to potential changes; instead, a very slow and gradual increase in oxidation state over time was observed (top panel in Fig. 3b).

This difference between the time-resolved optical and Ir-L_3 edge XAS spectroscopies suggests that while redox transitions 1 and 2 are associated with the oxidation of iridium, the third transition does not involve further oxidation of iridium. These findings resolve uncertainties present in steady-state spectral analysis regarding whether iridium continues to oxidise beyond a certain potential in small fraction that is beyond the detection limit, showing no dynamically dependent change in the oxidation state of iridium during the third redox transition. The observed slow increase in fluorescence intensity over time could indicate time-dependent oxidation of a small amount of bulk iridium, inaccessible within shorter experimental timeframes. Similar measurements on the dynamics of oxygen species reveal that the

fluorescence intensity at 529 eV of oxygen species does not change at potential range of 0.62 to 0.82 V_{RHE}, but rapidly increase and decrease with potential steps in the ranges of 1.1 to 1.27 V_{RHE} and 1.32 to 1.52 V_{RHE} (Fig. 3c). This behaviour aligns with the changes observed during CVs, as shown in Fig. 2c. Further investigations into these dynamics across various X-ray energies show that the observed changes are indeed sensitive to the selected X-ray beam energy (Fig. S13), confirming the changes are related to alterations in the oxygen species.

Integrating experimental findings and DFT calculations, the first redox transition are connected to Ir^{3+} to Ir^{4+} transitions and a deprotonation of water into *OH on Ir CUS site. This H_2O to *OH step is consistent with recent findings from Mom et al, who suggested based on DFT calculations that *OH on CUS Ir site is hardly visible in O-K-edge NEXAFS spectra.[52] The second redox transition can be associated with further oxidation from Ir^{4+} towards Ir^{5+}, as well as a deprotonation of *OH on bridge site into *O. This *OH to *O transformation was captured by the absorption peak at around 529.3 eV in O-K-edge NEXAFS spectra, aligned with prior O-K-edge NEXAFS observations.[25, 32, 36-39, 50-52, 54] The final redox transition, occurring in the OER-relevant potential region, involves further oxidation, and deprotonation of *OH at the CUS site to form $*O^{-1}$, while Ir remains at Ir^{5+}. This is consistent with our DFT calculations showing that electron depletion in this step is dominated by the oxygen ligand. This assignment is different from oxygen redox that emphasises lattice oxygen involvement, such as anion redox in battery cathodes and lattice oxygen evolution mechanism in OER.[55] In that context, a broad range of lattice oxygen atoms—including both bulk oxygen and surface bridge oxygen in a model rutile IrO_2 structure—may be active in redox transitions, which contributes to the capacity of battery or activity of catalysts, but poses stress to the stability of the materials. [56]

Kinetics of O^{-1} species for water oxidation

Although we have established that oxidising species Ir^{5+} and O^{-1} co-exist at high potentials, it remains unclear whether Ir^{5+}, O^{-1}, or a cooperative interaction between them controls the rate-determining O–O bond-forming step. To investigate the role of the accumulated oxidising species Ir^{4+}, Ir^{5+} and O^{-1} in catalysing water oxidation, we determined their decay time constants by coupling open-circuit-potential (OCP) decay measurements with time-resolved optical and X-ray spectroscopies. In this method, the potential is stepped up and held before switching to open circuit, allowing the electrode to relax (Fig. 4a). Fig. 4b shows that across all three potential regions examined, the fluorescence intensity of Ir remains stable after switching to open circuit, indicating that the accumulated Ir^{4+} and Ir^{5+} species are stable under open-circuit conditions. In contrast, the oxygen fluorescence signals at higher potentials (1.32 to 1.52 V_{RHE})—assigned to O^{-1} species—exhibit notable decay, suggesting consumption of these oxygen species during open-circuit conditions (Fig. 4c). It's worth noting that these dynamic behaviours of iridium and oxygen species were clearly observed using time-resolved optical spectroscopy. The optical signals corresponding to Ir^{4+} and Ir^{5+} remains constant, while the signal for O^{-1} states rapidly decays upon switching to open circuit (Fig. 4d). The decay rate increases with applied potential, indicating

quicker consumption of O^{-1} species at higher potentials, and thus at higher coverages of the O^{-1} states. (Fig. 4e). Similar trends were observed in time-resolved oxygen O-K edge absorption spectroscopy (Fig. S14). The stark difference in the behavior of highly oxidised Ir species and electron-deficient O^{-1} species, as evidenced by both optical and X-ray spectroscopies, suggests that although Ir is highly oxidised, it does not change oxidation state under OER conditions; instead, the O^{-1} is dynamically changing under the same conditions. We thus hypothesise that the fast kinetics of O–O bond formation and oxygen molecule release on iridium oxide, can be attributed to the accumulation of O^{-1} species at high potentials, resulting from the high covalency of Ir-O upon oxidation (as schematically shown in Fig. 4f).

To further understand the correlation between O^{-1} and oxygen evolution, we quantified oxygen release during OCP decay using highly sensitive on-chip electrochemical mass spectrometry (EC-MS), which allows in situ measurement of gas products during electrochemistry with sub-picomole-per-second resolution.[57, 58] Oxygen signals were measured using two sequential procedures: an OCP decay measurement and a step potential measurement as a control (see Supplementary note 6 for details). Notably, the OCP decay measurement shows a larger oxygen signal compared to the step potential measurement, indicating additional oxygen release during open-circuit decay (Fig. 4g). Reversing the order of the two procedures yielded consistent results—measurement with OCP decay yields higher oxygen amount, confirming that extra oxygen is released under open-circuit conditions, although no eternal currents can be detected (Fig. S15).We quantified the additional oxygen released during OCP decay by comparing the detected oxygen between the two measurements (see Supplementary Note 6 and Fig S16 for details). Measurements at potentials from 1.44 to 1.48 V_{RHE}, conducted in two independent experiments, consistently showed increased oxygen release during OCP decay (Fig. S17-18). Interestingly, the net amount of oxygen produced during OCP decay exhibits a strong correlation with the potentials applied before switching to open circuit, showing an almost linear increase with the applied potential in the studied region. Similar linear relation is observed for the accumulation of O^{-1} species and the applied potential in the same region, although with different concentration vs potential slopes (Fig. 4h) (see details of quantification of O^{-1} species in Fig. S19). Notably, the O^{-1} concentration is approximately 4 times the amount of oxygen released during OCP decay, which indicates the release of each oxygen molecule is associated with the consumption of four O^{-1} species. Specifically, the release of every O_2 from water molecules gives rise to 4 electrons to discharge four accumulated O^{-1} species. These results indicate that the consumption or decay of O^{-1} is quantitatively linked to the release of oxygen during open circuit decay, suggesting that O^{-1} species could be involved in the step of forming O-O bond and release oxygen.

On the basis of previous established DFT calculations for IrO_2 (110) surfaces—which suggest that the transition from *O to *OOH (i.e. O-O bond formation) is the rate-determining step of the reaction[24, 25, 43, 44]—we propose a mechanism for the open-circuit potential decay process, analogous to our previous work.[24] In this mechanism, an active site (O^{-1}) undergoes nucleophilic attack by a water molecule, leading to O–O bond formation and subsequent oxygen release. To maintain charge balance without

external electron transfer (as occurs during open-circuit conditions), other O^{-1} species in the network accept a proton and become reduced, regenerating O^{-2} in the form of *OH on the surface. While this mechanism is specific to the open-circuit potential decay, it involves a fundamental catalytic cycle with charged surface oxygen species (O^{-1}), water molecules, O–O bond formation and oxygen release. The key distinction between OCP decay and constant potential operation is the presence of an externally applied potential during the latter, which facilitates continuous electron extraction from the catalyst. This external potential enables the rapid reoxidation of reduced O^{-2} sites back to O^{-1} species, allowing them to participate in successive catalytic cycles releasing O_2. Therefore, we consider the mechanism described for OCP decay representing a single catalytic cycle of the OER on iridium oxides. Under constant potential/current operation, the OER is essentially a rapid succession of these cycles, with O^{-2} oxidation and O^{-1} species reformation occurring continuously, driving sustained oxygen evolution.

Our findings suggest that the critical rate-determining step of the OER — O–O bond formation—may proceed at surface oxygen ligand sites via highly oxidised O^{-1} species. Under anodic polarisation, the progressive oxidation of iridium enhances Ir–O covalency and brings the Ir-5d and O-2p band centres into closer energetic alignment, thereby promoting electron depletion from surface oxygen atoms and enabling the formation of O^{-1} species necessary for driving O–O bond formation. We propose that the ability of iridium oxides to stabilise such electron-deficient oxygen states arises from the unique covalency of surface Ir–O bonds under high potentials—a property that may be fundamental to their exceptionally fast OER kinetics. Recent studies, including our own,[23-25, 59] suggest based on DFT and experimental electro-adsorption isotherms that repulsive interactions exist between oxo species, which can lower the activation barrier of the rate-determining step and thus promote water oxidation. Our observations further highlight that these oxo species are intrinsically electron-deficient and highly reactive, and their repulsive interactions could be particularly critical in light of this electronic nature. As these reactive O^{-1} configurations are accessible only under operando conditions, our results underscore that an accurate understanding of catalytic activity should account for the electronic structure of the oxidised surface under very positive potential, rather than relying solely on bulk stoichiometric models commonly used in theoretical studies. As a result, future research focused on tuning surface metal–oxygen covalency and band alignment at high potentials can open promising avenues for the design of more active OER catalysts.

Conclusion

In summary, we have used multimodal, time-resolved spectroscopies to elucidate the potential-dependent oxidation states of iridium metal centre and oxygen ligands and their implications on the active states and reaction mechanism for water oxidation. We found a sequential oxidation processes of iridium oxides with increasing potential, which first involves iridium centre oxidation (Ir^{3+}/Ir^{4+} and Ir^{4+}/Ir^{5+}) at low potentials, then switches toward depleting electrons from oxygen ligands at higher potential, primarily due to the increased covalency of Ir-O, leading to the formation of electrophilic

oxygen O^{-1} at OER potential region. Time-resolved spectroscopies show that the time constant, or lifetime, of oxidised iridium (Ir^{5+}) is much longer than the oxygen release time constant, whereas the kinetics of electrophilic oxygen O^{-1} align closely with those of OER. These suggest that electrophilic oxygen, rather than the highly oxidised iridium, plays a key role in driving RDS–O-O bond formation in OER. Electrochemical mass spectrometry results show that the concentration of O^{-1} species is quantitatively correlated to the amount of molecular oxygen released, with consumption of roughly four O^{-1} for the release of every oxygen molecule. These results demonstrate the necessity of multimodal, time-resolved characterisation techniques to gain holistic understanding of complex solid-liquid interfaces and advance fundamental understanding of electrocatalytic processes. Beyond OER on metal oxides, identifying potential-dependent oxidation states and their dynamics serves as an important tool to determine how charge transfer occurs during rate-determining catalytic steps and probe the reactivity, selectivity and stability of active sites for a number of reactions such as CO_2 reduction, and oxygen reduction.

Declarations

Data availability

The Spectroscopic data were analysed by *Matlab* and *Python*, the deconvolution of absorption spectra was analysed using *Julia* programming language. Electrochemical mass spectrometry data were analysed in *Python* based on an open-source package *IXDAT* (https://ixdat.readthedocs.io/en/latest/). The data and analysis scripts will be openly available at https://github.com/Caiwu-L/IrOx_optical_vs_X-ray-spectroscopy.

Acknowledgements

C.L., I.E.L.S., J.R.D., R.R.R, S.J.H and M.T would like to acknowledge the funding and technical support from BP through the BP International Centre for Advanced Materials (bp-ICAM). C.L. also acknowledges the Imperial College London and China Scholarship Council for the IC-CSC joint scholarship. We acknowledge Diamond Light Source for time on Beamline B07 under Proposal SI34803 and Beamline B18 under Proposal SP30396 and SP31886. This project was supported by the Royal Academy of Engineering under the Research Fellowship program (R.R.R.). This work was also supported by the Engineering and Physical Sciences Research Council [EP/W033232/1]. Y.W. acknowledges the support from EPSRC and SFI Centre for Doctoral Training in Advanced Characterisation of Materials (Grant Ref: EP/S023259/1). S.K. and G.H. thank Horizon 2020 Grant 101017928 (HYSOLCHEM project) for funding. Via our membership of the UK's HEC Materials Chemistry Consortium, which is funded by EPSRC (EP/X035859/1), this work used the ARCHER2 UK National Supercomputing Service (http://www.archer2.ac.uk). TEM access was supported by the Henry Royce Institute for Advanced Materials, funded through EPSRC grants EP/R00661X/1, EP/S019367/1, EP/P025021/1 and EP/P025498/1.

Competing interests

The authors declare no competing interests.

References

1. McNaught, A. D.; Wilkinson, A. *Compendium of chemical terminology*; Blackwell Science Oxford, 1997.
2. Walsh, A.; Sokol, A. A.; Buckeridge, J.; Scanlon, D. O.; Catlow, C. R. A. Oxidation states and ionicity. *Nature Materials* **2018**, *17* (11), 958-964. DOI: 10.1038/s41563-018-0165-7.
3. Walsh, A.; Sokol, A. A.; Buckeridge, J.; Scanlon, D. O.; Catlow, C. R. A. Electron Counting in Solids: Oxidation States, Partial Charges, and Ionicity. *The Journal of Physical Chemistry Letters* **2017**, *8* (9), 2074-2075. DOI: 10.1021/acs.jpclett.7b00809.
4. Kuznetsov, D. A.; Han, B.; Yu, Y.; Rao, R. R.; Hwang, J.; Román-Leshkov, Y.; Shao-Horn, Y. Tuning Redox Transitions via Inductive Effect in Metal Oxides and Complexes, and Implications in Oxygen Electrocatalysis. *Joule* **2018**, *2* (2), 225-244. DOI: 10.1016/j.joule.2017.11.014.
5. Luo, K.; Roberts, M. R.; Hao, R.; Guerrini, N.; Pickup, D. M.; Liu, Y.-S.; Edström, K.; Guo, J.; Chadwick, A. V.; Duda, L. C.; et al. Charge-compensation in 3d-transition-metal-oxide intercalation cathodes through the generation of localized electron holes on oxygen. *Nature Chemistry* **2016**, *8* (7), 684-691. DOI: 10.1038/nchem.2471.
6. House, R. A.; Marie, J.-J.; Pérez-Osorio, M. A.; Rees, G. J.; Boivin, E.; Bruce, P. G. The role of O2 in O-redox cathodes for Li-ion batteries. *Nature Energy* **2021**, *6* (8), 781-789. DOI: 10.1038/s41560-021-00780-2.
7. Marie, J.-J.; House, R. A.; Rees, G. J.; Robertson, A. W.; Jenkins, M.; Chen, J.; Agrestini, S.; Garcia-Fernandez, M.; Zhou, K.-J.; Bruce, P. G. Trapped O2 and the origin of voltage fade in layered Li-rich cathodes. *Nature Materials* **2024**, *23* (6), 818-825. DOI: 10.1038/s41563-024-01833-z.
8. Sathiya, M.; Rousse, G.; Ramesha, K.; Laisa, C. P.; Vezin, H.; Sougrati, M. T.; Doublet, M. L.; Foix, D.; Gonbeau, D.; Walker, W.; et al. Reversible anionic redox chemistry in high-capacity layered-oxide electrodes. *Nature Materials* **2013**, *12* (9), 827-835. DOI: 10.1038/nmat3699.
9. Assat, G.; Tarascon, J.-M. Fundamental understanding and practical challenges of anionic redox activity in Li-ion batteries. *Nature Energy* **2018**, *3* (5), 373-386. DOI: 10.1038/s41560-018-0097-0.
10. Gao, X.; Li, B.; Kummer, K.; Geondzhian, A.; Aksyonov, D. A.; Dedryvère, R.; Foix, D.; Rousse, G.; Ben Yahia, M.; Doublet, M.-L.; et al. Clarifying the origin of molecular O2 in cathode oxides. *Nature Materials* **2025**. DOI: 10.1038/s41563-025-02144-7.
11. Lunger, J. R.; Karaguesian, J.; Chun, H.; Peng, J.; Tseo, Y.; Shan, C. H.; Han, B.; Shao-Horn, Y.; Gómez-Bombarelli, R. Towards atom-level understanding of metal oxide catalysts for the oxygen evolution reaction with machine learning. *npj Computational Materials* **2024**, *10* (1). DOI: 10.1038/s41524-024-01273-y.

12. Haase, F. T.; Ortega, E.; Saddeler, S.; Schmidt, F.-P.; Cruz, D.; Scholten, F.; Rüscher, M.; Martini, A.; Jeon, H. S.; Herzog, A.; et al. Role of Fe decoration on the oxygen evolving state of Co3O4 nanocatalysts. *Energy & Environmental Science* **2024**, *17* (5), 2046-2058, 10.1039/D3EE02809G. DOI: 10.1039/D3EE02809G.
13. Hubert, M. A.; Gallo, A.; Liu, Y.; Valle, E.; Sanchez, J.; Sokaras, D.; Sinclair, R.; King, L. A.; Jaramillo, T. F. Characterization of a Dynamic Y2Ir2O7 Catalyst during the Oxygen Evolution Reaction in Acid. *The Journal of Physical Chemistry C* **2022**, *126* (4), 1751-1760. DOI: 10.1021/acs.jpcc.1c07760.
14. Yang, F.; Jiang, S.; Liu, S.; Beyer, P.; Mebs, S.; Haumann, M.; Roth, C.; Dau, H. Dynamics of bulk and surface oxide evolution in copper foams for electrochemical CO2 reduction. *Communications Chemistry* **2024**, *7* (1), 66. DOI: 10.1038/s42004-024-01151-0.
15. Suntivich, J.; Hautier, G.; Dabo, I.; Crumlin, E. J.; Kumar, D.; Cuk, T. Probing intermediate configurations of oxygen evolution catalysis across the light spectrum. *Nature Energy* **2024**, *9* (10), 1191-1198. DOI: 10.1038/s41560-024-01583-x.
16. Rossmeisl, J.; Qu, Z. W.; Zhu, H.; Kroes, G. J.; Nørskov, J. K. Electrolysis of water on oxide surfaces. *Journal of Electroanalytical Chemistry* **2007**, *607* (1-2), 83-89. DOI: 10.1016/j.jelechem.2006.11.008.
17. Man, I. C.; Su, H.-Y.; Calle-Vallejo, F.; Hansen, H. A.; Martínez, J. I.; Inoglu, N. G.; Kitchin, J.; Jaramillo, T. F.; Nørskov, J. K.; Rossmeisl, J. Universality in Oxygen Evolution Electrocatalysis on Oxide Surfaces. *ChemCatChem* **2011**, *3* (7), 1159-1165. DOI: https://doi.org/10.1002/cctc.201000397 (acccessed 2024/06/21).
18. Nørskov, J. K.; Rossmeisl, J.; Logadottir, A.; Lindqvist, L.; Kitchin, J. R.; Bligaard, T.; Jonsson, H. Origin of the overpotential for oxygen reduction at a fuel-cell cathode. *The Journal of Physical Chemistry B* **2004**, *108* (46), 17886-17892.
19. McCrory, C. C. L.; Jung, S.; Peters, J. C.; Jaramillo, T. F. Benchmarking Heterogeneous Electrocatalysts for the Oxygen Evolution Reaction. *Journal of the American Chemical Society* **2013**, *135* (45), 16977-16987. DOI: 10.1021/ja407115p.
20. Geiger, S.; Kasian, O.; Ledendecker, M.; Pizzutilo, E.; Mingers, A. M.; Fu, W. T.; Diaz-Morales, O.; Li, Z.; Oellers, T.; Fruchter, L.; et al. The stability number as a metric for electrocatalyst stability benchmarking. *Nature Catalysis* **2018**, *1* (7), 508-515. DOI: 10.1038/s41929-018-0085-6.
21. Cherevko, S.; Geiger, S.; Kasian, O.; Kulyk, N.; Grote, J.-P.; Savan, A.; Shrestha, B. R.; Merzlikin, S.; Breitbach, B.; Ludwig, A.; et al. Oxygen and hydrogen evolution reactions on Ru, RuO2, Ir, and IrO2 thin film electrodes in acidic and alkaline electrolytes: A comparative study on activity and stability. *Catalysis Today* **2016**, *262*, 170-180. DOI: https://doi.org/10.1016/j.cattod.2015.08.014.
22. Naito, T.; Shinagawa, T.; Nishimoto, T.; Takanabe, K. Recent advances in understanding oxygen evolution reaction mechanisms over iridium oxide. *Inorganic Chemistry Frontiers* **2021**, *8* (11), 2900-2917. DOI: 10.1039/d0qi01465f.
23. Liang, C.; Katayama, Y.; Tao, Y.; Morinaga, A.; Moss, B.; Celorrio, V.; Ryan, M.; Stephens, I. E. L.; Durrant, J. R.; Rao, R. R. Role of Electrolyte pH on Water Oxidation for Iridium Oxides. *Journal of the American Chemical Society* **2024**, *146* (13), 8928-8938. DOI: 10.1021/jacs.3c12011.

24. Liang, C.; Rao, R. R.; Svane, K. L.; Hadden, J. H. L.; Moss, B.; Scott, S. B.; Sachs, M.; Murawski, J.; Frandsen, A. M.; Riley, D. J.; et al. Unravelling the effects of active site density and energetics on the water oxidation activity of iridium oxides. *Nature Catalysis* **2024**, *7* (7), 763-775. DOI: 10.1038/s41929-024-01168-7.
25. Nong, H. N.; Falling, L. J.; Bergmann, A.; Klingenhof, M.; Tran, H. P.; Spori, C.; Mom, R.; Timoshenko, J.; Zichittella, G.; Knop-Gericke, A.; et al. Key role of chemistry versus bias in electrocatalytic oxygen evolution. *Nature* **2020**, *587* (7834), 408-413. DOI: 10.1038/s41586-020-2908-2.
26. Kuo, D. Y.; Kawasaki, J. K.; Nelson, J. N.; Kloppenburg, J.; Hautier, G.; Shen, K. M.; Schlom, D. G.; Suntivich, J. Influence of Surface Adsorption on the Oxygen Evolution Reaction on IrO2(110). *J Am Chem Soc* **2017**, *139* (9), 3473-3479. DOI: 10.1021/jacs.6b11932.
27. Kwon, S.; Stoerzinger, K. A.; Rao, R.; Qiao, L.; Goddard, W. A., III; Shao-Horn, Y. Facet-Dependent Oxygen Evolution Reaction Activity of IrO2 from Quantum Mechanics and Experiments. *Journal of the American Chemical Society* **2024**, *146* (17), 11719-11725. DOI: 10.1021/jacs.3c14271.
28. Lu, B.; Wahl, C.; dos Reis, R.; Edgington, J.; Lu, X. K.; Li, R.; Sweers, M. E.; Ruggiero, B.; Gunasooriya, G. T. K. K.; Dravid, V.; et al. Key role of paracrystalline motifs on iridium oxide surfaces for acidic water oxidation. *Nature Catalysis* **2024**, *7* (8), 868-877. DOI: 10.1038/s41929-024-01187-4.
29. Saveleva, V. A.; Wang, L.; Teschner, D.; Jones, T.; Gago, A. S.; Friedrich, K. A.; Zafeiratos, S.; Schlögl, R.; Savinova, E. R. Operando Evidence for a Universal Oxygen Evolution Mechanism on Thermal and Electrochemical Iridium Oxides. *The Journal of Physical Chemistry Letters* **2018**, *9* (11), 3154-3160. DOI: 10.1021/acs.jpclett.8b00810.
30. Hillman, A. R.; Skopek, M. A.; Gurman, S. J. X-Ray spectroscopy of electrochemically deposited iridium oxide films: detection of multiple sites through structural disorder. *Phys. Chem. Chem. Phys.* **2011**, *13* (12), 5252-5263. DOI: 10.1039/c0cp01472a.
31. Diklić, N.; Clark, A. H.; Herranz, J.; Aegerter, D.; Diercks, J. S.; Beard, A.; Saveleva, V. A.; Chauhan, P.; Nachtegaal, M.; Huthwelker, T.; et al. Surface Ir+5 Formation as a Universal Prerequisite for O2 Evolution on Ir Oxides. *ACS Catalysis* **2023**, *13* (16), 11069-11079. DOI: 10.1021/acscatal.3c01448.
32. Nong, H. N.; Reier, T.; Oh, H.-S.; Gliech, M.; Paciok, P.; Vu, T. H. T.; Teschner, D.; Heggen, M.; Petkov, V.; Schlögl, R.; et al. A unique oxygen ligand environment facilitates water oxidation in hole-doped IrNiOx core–shell electrocatalysts. *Nature Catalysis* **2018**, *1* (11), 841-851. DOI: 10.1038/s41929-018-0153-y.
33. Velasco-Vélez, J.-J.; Carbonio, E. A.; Chuang, C.-H.; Hsu, C.-J.; Lee, J.-F.; Arrigo, R.; Hävecker, M.; Wang, R.; Plodinec, M.; Wang, F. R.; et al. Surface Electron-Hole Rich Species Active in the Electrocatalytic Water Oxidation. *Journal of the American Chemical Society* **2021**, *143* (32), 12524-12534. DOI: 10.1021/jacs.1c01655.
34. Li, A.; Kong, S.; Adachi, K.; Ooka, H.; Fushimi, K.; Jiang, Q.; Ofuchi, H.; Hamamoto, S.; Oura, M.; Higashi, K.; et al. Atomically dispersed hexavalent iridium oxide from MnO2 reduction for oxygen evolution catalysis. *Science* **2024**, *384* (6696), 666-670. DOI: 10.1126/science.adg5193 (acccessed 2025/03/06).

35. Retuerto, M.; Pascual, L.; Torrero, J.; Salam, M. A.; Tolosana-Moranchel, Á.; Gianolio, D.; Ferrer, P.; Kayser, P.; Wilke, V.; Stiber, S. Highly active and stable OER electrocatalysts derived from Sr2MIrO6 for proton exchange membrane water electrolyzers. *Nature communications* **2022**, *13* (1), 7935.
36. Pfeifer, V.; Jones, T. E.; Velasco Vélez, J. J.; Massué, C.; Arrigo, R.; Teschner, D.; Girgsdies, F.; Scherzer, M.; Greiner, M. T.; Allan, J.; et al. The electronic structure of iridium and its oxides. *Surface and Interface Analysis* **2016**, *48* (5), 261-273. DOI: 10.1002/sia.5895.
37. Pfeifer, V.; Jones, T. E.; Velasco Velez, J. J.; Massue, C.; Greiner, M. T.; Arrigo, R.; Teschner, D.; Girgsdies, F.; Scherzer, M.; Allan, J.; et al. The electronic structure of iridium oxide electrodes active in water splitting. *Phys Chem Chem Phys* **2016**, *18* (4), 2292-2296. DOI: 10.1039/c5cp06997a.
38. Pfeifer, V.; Jones, T. E.; Wrabetz, S.; Massue, C.; Velasco Velez, J. J.; Arrigo, R.; Scherzer, M.; Piccinin, S.; Havecker, M.; Knop-Gericke, A.; et al. Reactive oxygen species in iridium-based OER catalysts. *Chem Sci* **2016**, *7* (11), 6791-6795. DOI: 10.1039/c6sc01860b.
39. Pfeifer, V.; Jones, T. E.; Velasco Velez, J. J.; Arrigo, R.; Piccinin, S.; Havecker, M.; Knop-Gericke, A.; Schlogl, R. In situ observation of reactive oxygen species forming on oxygen-evolving iridium surfaces. *Chem Sci* **2017**, *8* (3), 2143-2149. DOI: 10.1039/c6sc04622c.
40. Klingenhof, M.; Trzesniowski, H.; Koch, S.; Zhu, J.; Zeng, Z.; Metzler, L.; Klinger, A.; Elshamy, M.; Lehmann, F.; Buchheister, P. W.; et al. High-performance anion-exchange membrane water electrolysers using NiX (X = Fe,Co,Mn) catalyst-coated membranes with redox-active Ni–O ligands. *Nature Catalysis* **2024**, *7* (11), 1213-1222. DOI: 10.1038/s41929-024-01238-w.
41. Zhang, R.; Pearce, P. E.; Pimenta, V.; Cabana, J.; Li, H.; Alves Dalla Corte, D.; Abakumov, A. M.; Rousse, G.; Giaume, D.; Deschamps, M.; et al. First Example of Protonation of Ruddlesden–Popper Sr_2IrO_4<: A Route to Enhanced Water Oxidation Catalysts. *Chemistry of Materials* **2020**, *32* (8), 3499-3509. DOI: 10.1021/acs.chemmater.0c00432.
42. Frati, F.; Hunault, M. O. J. Y.; de Groot, F. M. F. Oxygen K-edge X-ray Absorption Spectra. *Chemical Reviews* **2020**, *120* (9), 4056-4110. DOI: 10.1021/acs.chemrev.9b00439.
43. Ping, Y.; Nielsen, R. J.; Goddard, W. A., III. The Reaction Mechanism with Free Energy Barriers at Constant Potentials for the Oxygen Evolution Reaction at the IrO2 (110) Surface. *Journal of the American Chemical Society* **2017**, *139* (1), 149-155. DOI: 10.1021/jacs.6b07557.
44. Dickens, C. F.; Kirk, C.; Nørskov, J. K. Insights into the Electrochemical Oxygen Evolution Reaction with ab Initio Calculations and Microkinetic Modeling: Beyond the Limiting Potential Volcano. *The Journal of Physical Chemistry C* **2019**, *123* (31), 18960-18977. DOI: 10.1021/acs.jpcc.9b03830.
45. Tripathi, A.; Ocampo-Restrepo, V. K.; Norskov, J. K.; Kastlunger, G. Field effects explain the unintuitive potential response of electrochemical oxygen evolution in acid. *RSC Sustainability* **2025**. DOI: 10.1039/d5su00080g.
46. Petit, M. A.; Plichon, V. Anodic electrodeposition of iridium oxide films. *Journal of Electroanalytical Chemistry* **1998**, *444* (2), 247-252. DOI: https://doi.org/10.1016/S0022-0728(97)00570-6.
47. Wernet, P.; Nordlund, D.; Bergmann, U.; Cavalleri, M.; Odelius, M.; Ogasawara, H.; Näslund, L. Å.; Hirsch, T. K.; Ojamäe, L.; Glatzel, P.; et al. The Structure of the First Coordination Shell in Liquid Water.

Science **2004**, *304* (5673), 995-999. DOI: doi:10.1126/science.1096205.

48. Myneni, S.; Luo, Y.; Näslund, L. Å.; Cavalleri, M.; Ojamäe, L.; Ogasawara, H.; Pelmenschikov, A.; Ph, W.; Väterlein, P.; Heske, C.; et al. Spectroscopic probing of local hydrogen-bonding structures in liquid water. *Journal of Physics: Condensed Matter* **2002**, *14* (8), L213. DOI: 10.1088/0953-8984/14/8/106.
49. Mo, Y.; Stefan, I. C.; Cai, W.-B.; Dong, J.; Carey, P.; Scherson, D. A. In Situ Iridium LIII-Edge X-ray Absorption and Surface Enhanced Raman Spectroscopy of Electrodeposited Iridium Oxide Films in Aqueous Electrolytes. *The Journal of Physical Chemistry B* **2002**, *106* (14), 3681-3686. DOI: 10.1021/jp014452p.
50. Drevon, D.; Görlin, M.; Chernev, P.; Xi, L.; Dau, H.; Lange, K. M. Uncovering The Role of Oxygen in Ni-Fe(OxHy) Electrocatalysts using In situ Soft X-ray Absorption Spectroscopy during the Oxygen Evolution Reaction. *Scientific Reports* **2019**, *9* (1), 1532. DOI: 10.1038/s41598-018-37307-x.
51. Van Der Heijden, O.; Eggebeen, J. J. J.; Trzesniowski, H.; Deka, N.; Golnak, R.; Xiao, J.; Van Rijn, M.; Mom, R. V.; Koper, M. T. M. Li+ Cations Activate NiFeOOH for Oxygen Evolution in Sodium and Potassium Hydroxide. *Angewandte Chemie International Edition* **2024**. DOI: 10.1002/anie.202318692.
52. Mom, R. V.; Falling, L. J.; Kasian, O.; Algara-Siller, G.; Teschner, D.; Crabtree, R. H.; Knop-Gericke, A.; Mayrhofer, K. J. J.; Velasco-Vélez, J.-J.; Jones, T. E. Operando Structure–Activity–Stability Relationship of Iridium Oxides during the Oxygen Evolution Reaction. *ACS Catalysis* **2022**, *12* (9), 5174-5184. DOI: 10.1021/acscatal.1c05951.
53. Frevel, L. J.; Mom, R.; Velasco-Vélez, J.-J.; Plodinec, M.; Knop-Gericke, A.; Schlögl, R.; Jones, T. E. In Situ X-ray Spectroscopy of the Electrochemical Development of Iridium Nanoparticles in Confined Electrolyte. *The Journal of Physical Chemistry C* **2019**, *123* (14), 9146-9152. DOI: 10.1021/acs.jpcc.9b00731.
54. Velasco Vélez, J. J.; Bernsmeier, D.; Jones, T. E.; Zeller, P.; Carbonio, E.; Chuang, C.-H.; Falling, L. J.; Streibel, V.; Mom, R. V.; Hammud, A.; et al. The rise of electrochemical NAPXPS operated in the soft X-ray regime exemplified by the oxygen evolution reaction on IrO_x electrocatalysts. *Faraday Discussions* **2022**, *236*, 103-125. DOI: 10.1039/d1fd00114k.
55. Grimaud, A.; Hong, W. T.; Shao-Horn, Y.; Tarascon, J. M. Anionic redox processes for electrochemical devices. *Nature Materials* **2016**, *15* (2), 121-126. DOI: 10.1038/nmat4551.
56. Scott, S. B.; Sørensen, J. E.; Rao, R. R.; Moon, C.; Kibsgaard, J.; Shao-Horn, Y.; Chorkendorff, I. The low overpotential regime of acidic water oxidation part II: trends in metal and oxygen stability numbers. *Energy & Environmental Science* **2022**, *15* (5), 1988-2001, 10.1039/D1EE03915F. DOI: 10.1039/D1EE03915F.
57. Trimarco, D. B.; Scott, S. B.; Thilsted, A. H.; Pan, J. Y.; Pedersen, T.; Hansen, O.; Chorkendorff, I.; Vesborg, P. C. K. Enabling real-time detection of electrochemical desorption phenomena with sub-monolayer sensitivity. *Electrochimica Acta* **2018**, *268*, 520-530. DOI: https://doi.org/10.1016/j.electacta.2018.02.060.

58. Scott, S. B.; Rao, R. R.; Moon, C.; Sørensen, J. E.; Kibsgaard, J.; Shao-Horn, Y.; Chorkendorff, I. The low overpotential regime of acidic water oxidation part I: the importance of O2 detection. *Energy & Environmental Science* **2022**, *15* (5), 1977-1987, 10.1039/D1EE03914H. DOI: 10.1039/D1EE03914H.

59. Risch, M.; Ringleb, F.; Kohlhoff, M.; Bogdanoff, P.; Chernev, P.; Zaharieva, I.; Dau, H. Water oxidation by amorphous cobalt-based oxides: in situ tracking of redox transitions and mode of catalysis. *Energy & Environmental Science* **2015**, *8* (2), 661-674, 10.1039/C4EE03004D. DOI: 10.1039/C4EE03004D.

Figures

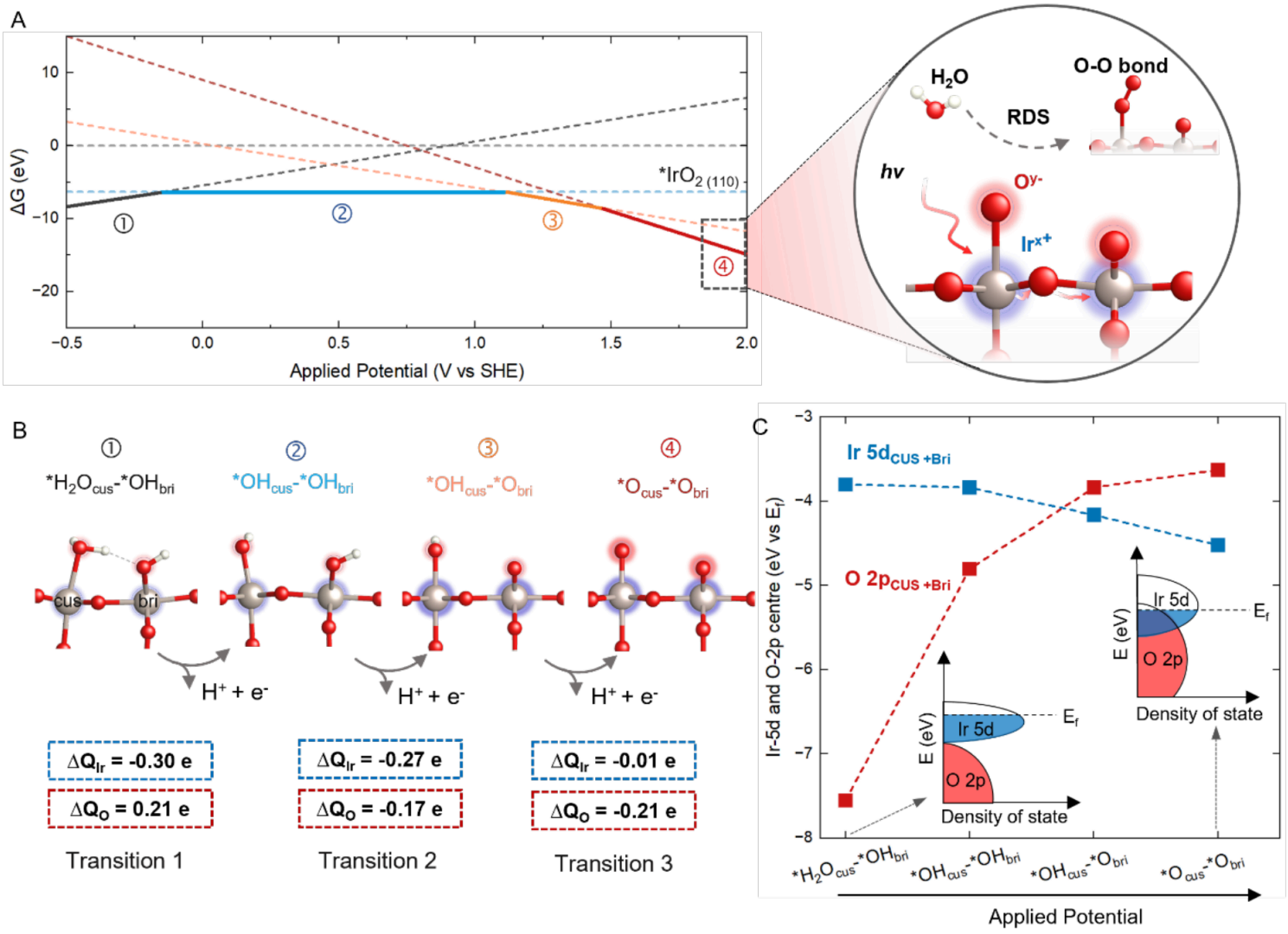


Figure 1

(A) Potential dependent coverage of adsorbates on a modelled IrO_2 structure from DFT calculations (left) and schematic showing the calculated structure before the rate determining step (RDS) of water oxidation—O-O bond formation, highlighting the ambiguous oxidation states and charge distribution for this critical intermediate (right). (B) Structures involved in different redox transitions from DFT calculations and the corresponding average change in Bader charges (ΔQ_{Ir} and ΔQ_O) for Ir and O atoms

present at IrO_2 surfaces during each redox reaction. Positive (negative) numbers indicate an increase (decrease) in the number of electrons (see detailed calculations in Supplementary Note 1). The blue and red shading surrounding iridium and oxygen atoms are a simple eye guide to indicate positive charge and negative charge, respectively, with the size and intensity of the shading reflecting the magnitude of charge change. (C) The average Ir 5d and O 2p band centre energies (*vs.* Fermi level) of surface atoms for different surface adsorbate structures (see separated band centres of CUS and Bri sites in Fig. S2). The inset scheme illustrates the shifting of the Ir 5d to lower energy and overlapping with oxygen 2p bands as the surface structure evolves with increasing applied potential (see projected density of states in Supplementary Note 1).

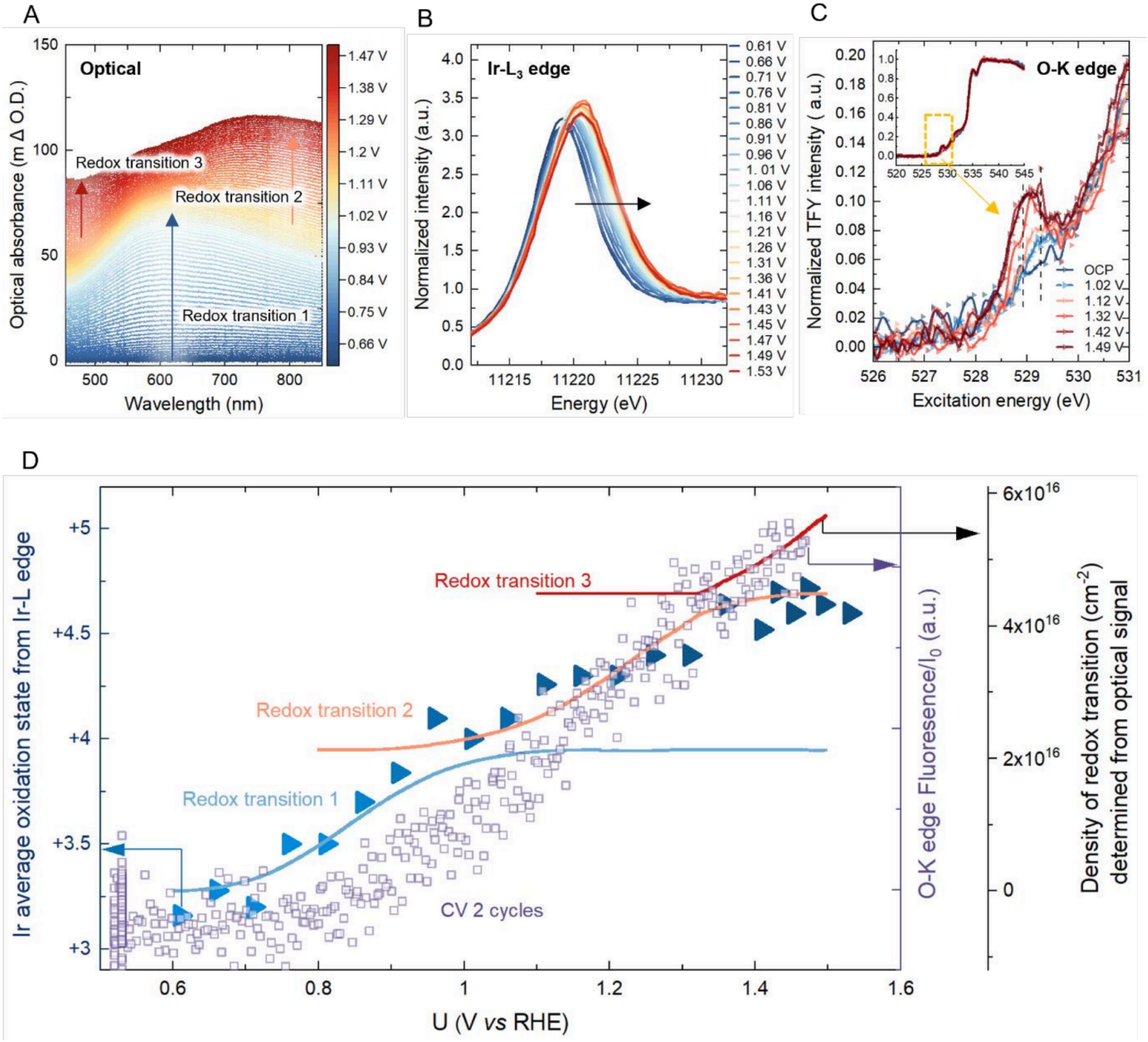


Figure 2

(A) Difference UV vis absorbance spectra of IrO_x during a linear sweep scan from 0.66 V_{RHE} to 1.48 V_{RHE} in 0.1M $HClO_4$ at a scan rate of 1 mV s^{-1} (iR corrected). The absorption changes are calculated with respect to the absorption at 0.66 V_{RHE}. Absorption changes were recorded after 5 CV cycles, at every 1 mV and shown at every 5 mV. Arrows indicate the dominant wavelengths where absorbance increases with potential, representing three different redox transitions (B) Ir L_3-edge XANES region of electrodeposited IrO_x on Fluorine-doped tin oxide (FTO) substrate measured at different potentials in 0.1 M $HClO_4$. Data adapted from our previous work[23] (C) Insets: steady-state operando NEXAFS O K-edge spectra of amorphous IrO_x deposited on gold-coated SiN_x substrates measured at various applied potentials in 0.1 M $HClO_4$ electrolyte. Potential values are given vs reversible hydrogen electrode (RHE) and OCP refers to open circuit potential. The data was normalised to the intensity at around 540 eV and calibrated using the pre-edge of water at 535 eV[47, 48] The main figure is a zoom in with energy from 526 to 531 eV. Dashed lines show two peak positions of around 528.9 eV and 529.3 eV increase with applied potentials. (D) Comparison between the iridium oxidation state determined from the white-line position in (B) (left y-axis), the deconvoluted densities of redox transitions 1, 2, and 3 from optical spectroscopy (black, right y-axis), and the fluorescence intensity at 529 eV in the O K-edge over two CV cycles. The y-axis scales are adjusted for visual clarity.

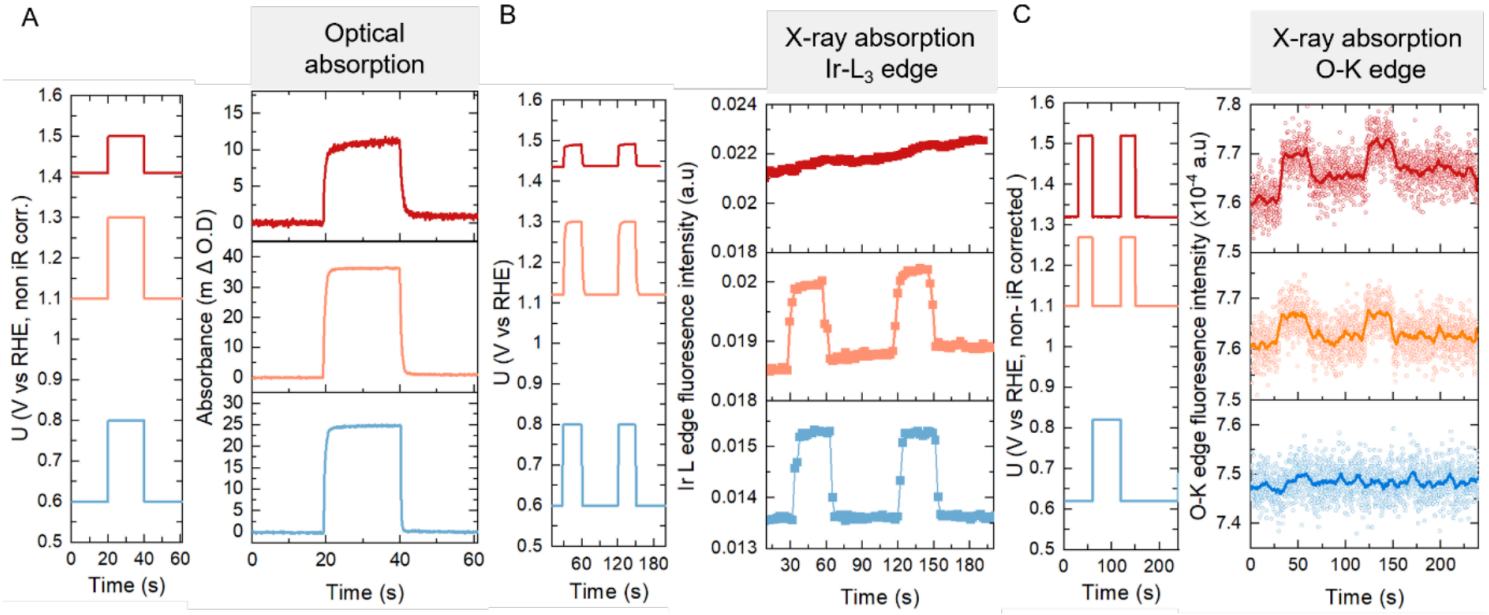


Figure 3

(A) Time-resolved optical absorption changes during potential step experiments on IrO□ in 0.1 M $HClO_4$ electrolyte. Potentials (non-iR-corrected) were stepped from 0.6–0.8 V_{RHE}, 1.1–1.3 V_{RHE}, and 1.41–1.5 V_{RHE}. Optical absorption was monitored at wavelengths of 600 nm, 800 nm, and 500 nm, corresponding to the maximum absorption wavelength for redox transitions 1, 2, and 3, respectively (see Fig. S5). (B) Changes in fluorescence intensity at the Ir L_3-edge (11222 eV) during potential step experiments on IrO□ deposited on an FTO substrate in 0.1 M $HClO_4$ electrolyte. Potential steps were applied between 0.6–0.8 V_{RHE}, 1.12–1.3 V_{RHE}, and 1.44–1.5 V_{RHE}, corresponding to redox transitions 1, 2,

and 3, respectively, as identified from spectral deconvolution in optical spectroscopy. (C) Changes in fluorescence intensity at the O K-edge during potential step experiments in 0.1 M $HClO_4$ electrolyte. Potentials (non-iR-corrected) were stepped in the ranges of 0.62–0.82 V_{RHE}, 1.1–1.27 V_{RHE}, and 1.32–1.52 V_{RHE}. Fluorescence intensity changes were monitored at 529 eV for the potential ranges 0.62–0.82 V_{RHE} and 1.1–1.27 V_{RHE}, and at 528.7 eV for the range 1.32–1.52 V_{RHE}.

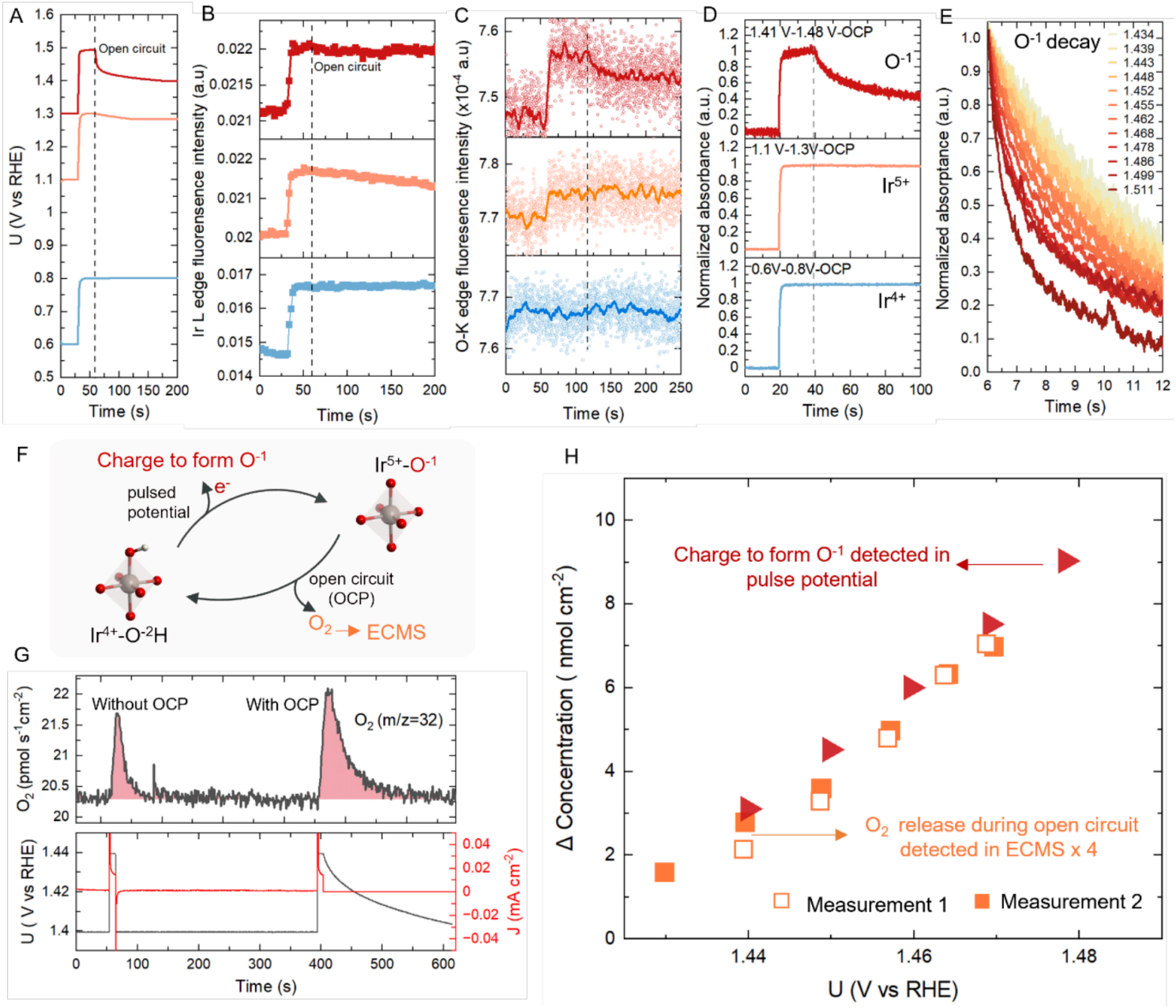


Figure 4

(A) Potential profile of open circuit potential decay measurement for potential ranges of 0.6-0.8 V_{RHE}, 1.12-1.3 V_{RHE} and 1.3-1.5 V_{RHE} for IrO_x on FTO in 0.1 M $HClO_4$ electrolyte. (B) Change in fluorescence intensity of Ir L edge (11222 eV) during open circuit potential decay measurement (C) Change in fluorescence intensity of O-K edge during open circuit decay measurement at 529 eV for 0.62-0.82 V_{RHE} and 1.1-1.27 V_{RHE}, and 528.7 eV for 1.27-1.52 V_{RHE}. (D)The normalized optical signal decay as a function

of time in an open circuit decay measurement for IrO_x on FTO in 0.1 M $HClO_4$ electrolyte. Optical signals are taken at maximum absorption wavelength for each forming oxidized states, with Ir^{4+} at 600 nm, Ir^{5+} at 800 nm, and O^{-1} at 500 nm. (E) Normalized optical signal decay at the wavelength of 500 nm as a function of time with different applied potentials. The potentials are iR corrected and in RHE scale. (F) Schematic showing the formation of O^{-1} on removing electron and proton on a protonated IrO_6 structure by raising potentials and its corresponding decay during open circuit potential to form molecular oxygen. (G) O_2 (m/z = 32) detected in ECMS for pulsed potential measurements from 1.40 to 1.44 V_{RHE} and for a subsequent OCP decay measurement with the same pulsed potential steps and holding time. (H) Quantitative comparison between the charge required to generate O^{-1} species and the charge converted into molecular oxygen during open circuit potential OCP decay. The concentration of O^{-1} is determined by integrating the charge from the cathodic current peak observed during pulsed potential measurements, starting from 1.415 V_{RHE} to various higher potentials and back to 1.s415 $V_{RHE.}$ This cathodic peak indicates the charge required to reduce the accumulated O^{-1} back to O^{-2} at 1.415 V_{RHE}, assuming a one-to-one correspondence between O^{-1} formation and the number of electrons transferred, as above this potential, the charge passed is governed mainly by oxygen redox, with negligible contribution from iridium (see Fig. 2d). The amount of oxygen released at OCP is directly quantified by electrochemical mass spectrometry, with the amount of O_2 generated during the potential-jumping control subtracted (see Fig S16). The cathodic current spike, its integration and the corresponding oxygen amount in ECMS are shown in Fig. S19.

Supplementary Files

This is a list of supplementary files associated with this preprint. Click to download.

- SupportinginformationV6250628.docx